



HAL
open science

Broadband Reflecting Luneburg Lenses Based on Bed-of-Nails Metasurfaces

Christos Bilitos, Xavier Morvan, Enrica Martini, Ronan Sauleau, Stefano Maci, David González-Ovejero

► **To cite this version:**

Christos Bilitos, Xavier Morvan, Enrica Martini, Ronan Sauleau, Stefano Maci, et al.. Broadband Reflecting Luneburg Lenses Based on Bed-of-Nails Metasurfaces. *IEEE Transactions on Antennas and Propagation*, 2024, 72 (2), pp.1923-1928. 10.1109/TAP.2023.3341208 . hal-04467425

HAL Id: hal-04467425

<https://univ-rennes.hal.science/hal-04467425>

Submitted on 2 May 2024

HAL is a multi-disciplinary open access archive for the deposit and dissemination of scientific research documents, whether they are published or not. The documents may come from teaching and research institutions in France or abroad, or from public or private research centers.

L'archive ouverte pluridisciplinaire **HAL**, est destinée au dépôt et à la diffusion de documents scientifiques de niveau recherche, publiés ou non, émanant des établissements d'enseignement et de recherche français ou étrangers, des laboratoires publics ou privés.



Distributed under a Creative Commons Attribution - NonCommercial 4.0 International License

Communication

Broadband Reflecting Luneburg Lenses Based on Bed of Nails Metasurfaces

Christos Bilitos, *Student, IEEE*, Xavier Morvan, Enrica Martini, *Senior Member, IEEE*,

Ronan Sauleau, *Fellow, IEEE*, Stefano Maci, *Fellow, IEEE*, and David González-Ovejero, *Senior Member, IEEE*

Abstract—This paper describes the bandwidth (BW) characteristics of Reflecting Luneburg lenses (RLL) implemented by a bed-of-nails (BoN). RLLs beam-formers consist of two vertically stacked parallel plate waveguides (PPWs) of circular shape. The bottom PPW contains a graded index (GRIN) medium with azimuthal symmetry to address the rays launched by a point source on a focal line along curvilinear paths up to a corner reflector. After reflection and coupling, the rays emerge collimated in the top PPW. The lens' symmetry allows for generating plane waves with arbitrary directions by just changing the azimuthal position of the source in the bottom layer. The use of BoN with higher symmetries helps to synthesize the refractive index profile in the RLL, which also features high values, and increases its operational BW by mitigating frequency dispersion. A Ka-band RLL featuring higher symmetries has been fabricated and tested. Simulations and measurements are in good agreement, showing an overall fractional BW of $\approx 39\%$. This architecture constitutes a metal-only, low-profile beam-former with full azimuthal scanning from 26 GHz to 40 GHz.

Index Terms—beamformer, broadband, higher symmetries, Ka-band, metasurface, reflecting Luneburg lens.

I. INTRODUCTION

WIRELESS communications are evolving to bolster ubiquitous broadband access by merging terrestrial and satellite networks, especially in low Earth orbit (LEO) [1]. Terminals for land and airborne vehicles should be low-profile, easily deployable, offer beam agility, and address the increasing demand for data-driven applications by utilizing the wider bandwidths (BWs) available in K- and Ka-band systems. Phased arrays offer electronic beam steering with low profile structures, but they can be complex and costly in the millimeter wave range [2]. Alternatively, one can simultaneously point at different directions by cost-effective multi-beam quasi-optical (QO) systems in parallel plate waveguide (PPW). Among QO beam-formers, one finds pillbox systems [3], which consist of two stacked PPWs connected by a 180° PPW bend with parabolic profile. A primary feed at the focus of the parabola in the bottom parallel plate generates a plane wave in the upper PPW. Thus, one can obtain one beam per feed in the focal plane when the top PPW embodies a radiating aperture.

Manuscript received July 4, 2023; revised October 24, 2023. This work has been supported by the Agence de l'Innovation de Défense (AID), and by the European Union through the European Regional Development Fund (ERDF).

C. Bilitos, R. Sauleau, and D. González-Ovejero are with Univ. Rennes, CNRS, Institut d'Électronique et des Technologies du numérique (IETR), UMR 6164, 35000 Rennes, France (e-mail: david.gonzalez-ovejero@univ-rennes1.fr).

E. Martini and S. Maci are with Department of Information Engineering and Mathematics, University of Siena, Italy (e-mail: macis@dii.unisi.it).

Nonetheless, as the feed moves away from the focus of the reflector to steer the beam, the side-lobe level (SLL) swiftly increases owing to phase errors. Flat Luneburg [4]–[6] and Gutman lenses [7] may also provide a number of fan beams in azimuth (the direction of which is determined by the placements of the feed points) without exhibiting scan losses. Delay lenses based on shaped continuous PPWs can also provide low [8] or moderate [9] scan losses. Nevertheless, an antenna is needed after the lens and on its same plane to radiate pencil beams, which leads to a total footprint significantly larger than in pillbox systems [10].

Recently, Reflecting Luneburg lenses (RLL) have been introduced in [11] to benefit from the advantages of pillbox beam-formers and Luneburg lenses. On the one hand, they consist of a dual layer structure, so a common surface is shared between the beam-former and the antenna. On the other hand, the lens' cylindrical symmetry may enable full azimuthal scanning when the radiating aperture also presents cylindrical symmetry. The RLL's bottom PPW can be implemented by a delay lens as in [12] or by using a metasurface (MTS) to emulate the effect of a graded index (GRIN) medium [11], [13], [14]. This paper deals with the implementation of the GRIN medium by metal-only MTSs, since they are more robust to large thermal ranges and high radiation levels than those based on dielectric. Hence, they can better withstand harsh environments both in the ground and space segments.

The implementation of RLLs by metallic bed of nails was succinctly addressed in [11]. Nonetheless, the latter solution yielded good results only for relatively narrow BWs. To overcome this hurdle, we adopt unit-cells with glide symmetry. This concept was first investigated in the 60's and 70's [15], [16] and helps to mitigate dispersion, thus improving the BW of planar lenses [17], [18]. The practical implementation of metal-only RLLs by a bed of nails (BoN) structure has not been reported before in the literature. It is shown here, for the first time, that the synthesis of the RLL's graded index by means of BoN with higher symmetries allows one to achieve an impressive relative bandwidth of 39%, covering the entire Ka-band. Moreover, the beam-width, sidelobe levels, and cross polarization maintain a very good in-band performance.

This paper is organized as follows. Section II summarizes the properties of RLLs, whereas Section III presents the unit-cell choice for the realization of the GRIN medium. Section IV describes the configuration of the lens antenna and the simulation results. The antenna prototype design and the experimental results are discussed in Section V and conclusions are drawn in Section VI.

II. REFLECTING LUNEBURG LENSES

The GRIN medium in an RLL directs rays from a source at the periphery of the bottom PPW along curvilinear paths (white lines in Fig. 1(a)), such that, after reflection, they emerge parallel in the top PPW (black arrows in Fig. 1(a)). The refractive index profile granting this behaviour reads as [11]

$$n(r) = n_0 \left(\frac{-1 + \sqrt{1 + 8(r/R)^2}}{2((r/R)^2)} \right)^{3/2} \quad (1)$$

where n_0 is the refractive index of the upper PPW, r is the radial distance and R is the radius of the lens. The upper PPW layer is here filled with air ($n_0 = 1$), so $n(R) = 1$ and the rays reaching the rim of the bottom PPW can be efficiently reflected and coupled to the top PPW over a broad band by using the corner reflector shown in Fig. 1(d). This configuration greatly simplifies the fabrication compared to the designs in [11], [13], [14], which required an extremely thin ($\ll t$) middle metal plate for a proper operation. The additional optical path length added by the thickness t is accounted for by optimising d_h in Fig. 1(d).

The ray paths in the GRIN medium are also concentrated around an internal focal region, located at $r \approx 0.46R$. When the source is placed in this inner focal region, the effect of spherical aberrations is limited and the operation of the lens does not change significantly [11]. Hence, a plane wave is still generated in the upper PPW, as shown in Fig. 1(b). This configuration is of utmost importance in practical designs, since the sources and the corner reflector do not have to coexist any more in the focal circumference. This way, one avoids undesired coupling and a 360° scanning range in azimuth becomes possible. Fig. 1(c) shows such a configuration, with a circular array of rectangular open-ended waveguides placed at the inner focal region for multi-beam operation. Detailed section views of the 180° bend and the radiating long slot after the 90° bend in the top PPW are depicted in Fig. 1(d) and Fig. 1(e), respectively. In the following, we will focus on the realization of the GRIN medium in the bottom PPW and the coupling to the upper one for RLLs considering sources located on the internal focal region, as in Figs. 1(b) and (c).

Notwithstanding the benefits listed above, the realization of RLLs by using standard unit-cells may be an onerous task. Specifically, when (1) is solved for $r = 0$, the highest refractive index is $n(0) = 2\sqrt{2}$, a significant increase compared with other GRIN lenses such as the LL ($n_{max} = \sqrt{2}$) and the MFE ($n_{max} = 2$). This problem is mitigated when feeding from the inner focal region of the lens, since $n_{max} = 1.86$ for $r = 0.46R$. Nevertheless, the relatively high values of n_{max} restrict the number of unit-cells able to implement the RLL, especially when trying to maintain a metal-only design [19].

III. UNIT-CELL ANALYSIS

Metallic pillars on a ground plane, also known as bed of nails (BoN), are a promising candidate to implement the large refractive indexes in RLLs. However, this structure presents significant frequency dispersion and anisotropy, and

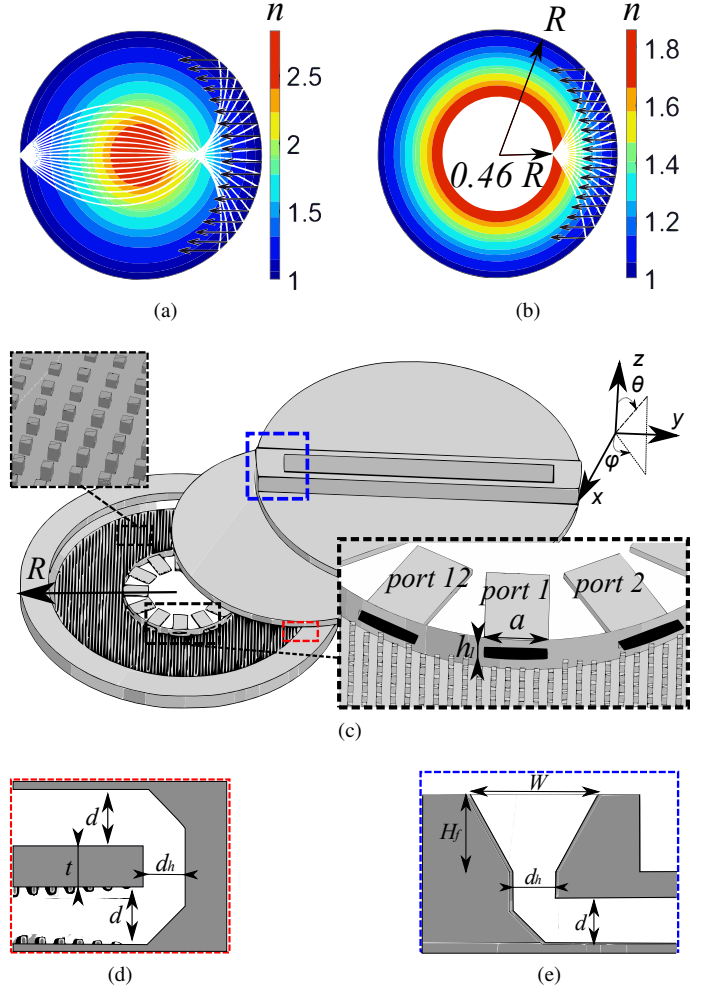


Fig. 1. Ray-paths in the RLL's GRIN medium and color map with the refractive index values for the conventional RLL when the source is placed (a) on its focal circumference and (b) on the inner caustic of the lens. (c) Exploded view of the RLL that utilizes the internal focal region, along with a close-up view of the open-ended waveguide used as feeder (with dimensions $a = 7.112$ mm and $h_1 = 1$ mm). Section views of (d) the 180° bend used to couple the power to the upper PPW and (e) the 90° bend used to radiate orthogonally to the RLL plane, with a flared vertical PPW section to ensure matching to free space. The dimensions are $d = 3.5$ mm, $d_h = 2.5$ mm, $t = 3$ mm, $W = 10.21$ mm and $H_f = 6$ mm.

it is characterized by a reduced frequency range with unimodal propagation of the fundamental transverse magnetic (TM) mode (necessary to avoid the excitation of higher order modes). To overcome this BW limitation, we explore BoN with mirror and glide symmetries [15]–[17], [20] obtained by mirroring and translating the unit-cell geometry by half of its periodicity. Doing so, one obtains larger variations of the equivalent refractive index, while achieving a linear variation of the phase constant. The dispersive behaviour is thus mitigated over a wide frequency range. Higher symmetric unit-cells formed by holes could be an alternative, but it is challenging to obtain with holes without dielectric loading an equivalent refractive index as high as 1.86 [21], [22]. Moreover, it has been shown that metallic pins are easily amenable for fabrication by additive manufacturing [19] and by micro-machining in the sub-THz range [23], so they are retained as the most suitable metal-only choice.

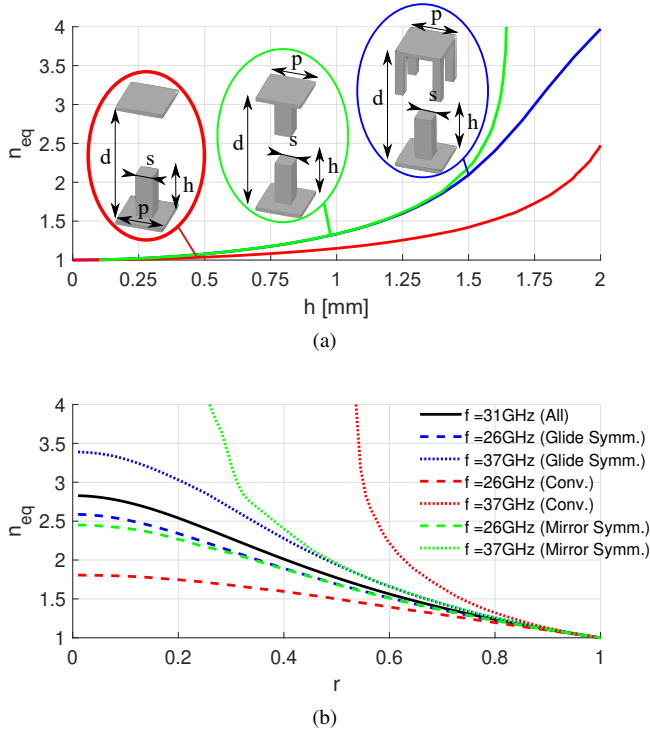


Fig. 2. (a) Equivalent refractive index as a function of the pin height h at 31 GHz for the unit-cell with glide symmetry (—), mirror symmetry (—) and its conventional counterpart (—), the dimensions are $s = 0.45$ mm, $p = 1.25$ mm and $d = 3.5$ mm in all cases. (b) Synthesized refractive index profile at different frequencies with with glide symmetry (---), mirror symmetry (---) and without higher symmetries (---).

In the remainder of this section we focus on BoN structures for RLLs at Ka band (26.5-40 GHz). To study the unit-cells' behaviour, we assume that they are embedded in a locally periodic environment with periodicity $p = 1.25$ mm and use an eigen mode solver with periodic boundary conditions [24]. For a propagation frequency f_0 of the fundamental mode, a phase shift ψ must be applied; the corresponding wavenumber β is calculated as $\beta = \psi/p$. Then, β is related to the effective refractive index as $\beta = k_0 n_{eq}$, where k_0 is the wavenumber of free space. Fig. 2(a) illustrates the effective refractive index obtained at $f_0 = 31$ GHz by varying the post height h for the classical BoN unit-cell (red line) and for its counterparts with mirror (green line) and glide symmetry (blue line). The other dimensions of the metallic inclusion are $s = 0.45$ mm, and $d = 3.5$ mm. It is clear that mirror and glide-symmetric unit cells allow one to implement higher n_{eq} than the conventional BoN for equivalent values of h .

As one moves away from the design frequency, the retrieved refractive index profile will vary due to dispersion. This translates in an increase of spherical aberrations due to the spreading and/or displacement of the focal region and leads to higher SLLs. In Fig. 2(b), the RLL refractive index profiles of a lens designed at 31 GHz are depicted also at 26 and 37 GHz. It is clear that, with the use of higher symmetries, the profiles at 26 and 37 GHz are much closer to the ideal profile at the design frequency. Therefore, a more stable operation in frequency is expected. The glide-symmetric configuration also exhibits reduced anisotropy, which is beneficial for the lens' rotationally symmetric operation.

IV. NUMERICAL RESULTS

This section presents full wave simulations for the RLL design in Fig. 1(c) at $f_0 = 31$ GHz. Both circular PPWs present a height $d = 3.5$ mm and a radius $R = 50$ mm or $5.2 \lambda_0$, where λ_0 is the free-space wavelength at f_0 . Compared to [13], the thickness of the middle plate has been increased to $t = 3$ mm (see Fig. 1(d)) to enable its machining. In turn, the corner reflector has been modified by introducing the dimension $d_h = 2.5$ mm to preserve the efficient coupling between the two PPWs. The two metallic plates forming the bottom PPW are loaded with the glide symmetric metallic unit-cell in Section II. The RLL's GRIN medium has been sampled according to a Cartesian lattice that accounts for the pillars on either plate of the PPW, which results in a sampling distance equal to half the unit-cell side. Next, each sample has been filled with the pillar dimensions that match the local refractive index in Fig. 2(a).

The lens is illuminated by twelve open-ended rectangular waveguides with width $a = 7.112$ mm and height $h_1 = 1$ mm, whose apertures are located at $r = 0.46R$. These dimensions yield an edge taper of 10 dB for a 42° illumination angle at the input of the lens and 61° illumination angle at the periphery of the lens. Given the symmetry of the structure the excitation of ports 1 and 2 in Fig. 1(c) (at an angle $\phi = 0^\circ$ and $\phi = 30^\circ$, respectively), suffices to fully characterize it. The height h of the bottom and top pins varies radially from 1.39 mm to 0.305 mm. A minimum distance between the top and bottom pins has been imposed, so the gap is sufficient to insert the feeding waveguide of height h_1 . The structure radiates orthogonally to the RLL plane through a rectangular 105 mm long and 10.21 mm wide slot. For that purpose, besides the 180° bend connecting the bottom and top PPW, an additional 90° bend has been included, as presented in Fig. 1(e). The PPW section between the 90° bend and the slot has been linearly flared to improve the matching to free space. CST's time-domain solver [24] has been used to simulate this structure.

Fig. 3(a) shows the magnitude (left) and phase distribution (right) of the vertical component of the electric field at 31 GHz in the top PPW. As expected, the latter image shows a neat plane wave in the upper PPW. Azimuthal scanning can be achieved through a combination of switching between the 12 ports in the bottom PPW (displayed in Fig. 3(b)) and the rotation of the top metal cover. Fig. 3(c) depicts the beams excited when the slot inclination with respect to the y -axis is 0° . In this instance, only ports 11, 12, 1, 2 and 3 each generate a beam in the visible region. Fig. 3(c) displays the case for a slot inclination of 30° , in which only ports 12, 1, 2, 3 and 4 contribute to the beam generation. To further demonstrate the scanning capabilities of the system, Fig. 3(e) represents the -3 dB contours for various slot orientations relative to the y -axis, ranging from 0° to 150° in increments of 30° ; it is shown that by carefully selecting the ports and slot orientation, one can achieve full azimuthal scanning for various elevation angles. The beam cross-over level in Fig. 3(c) may be increased by resorting to multiple feed per beam architectures as in [25] and references therein.

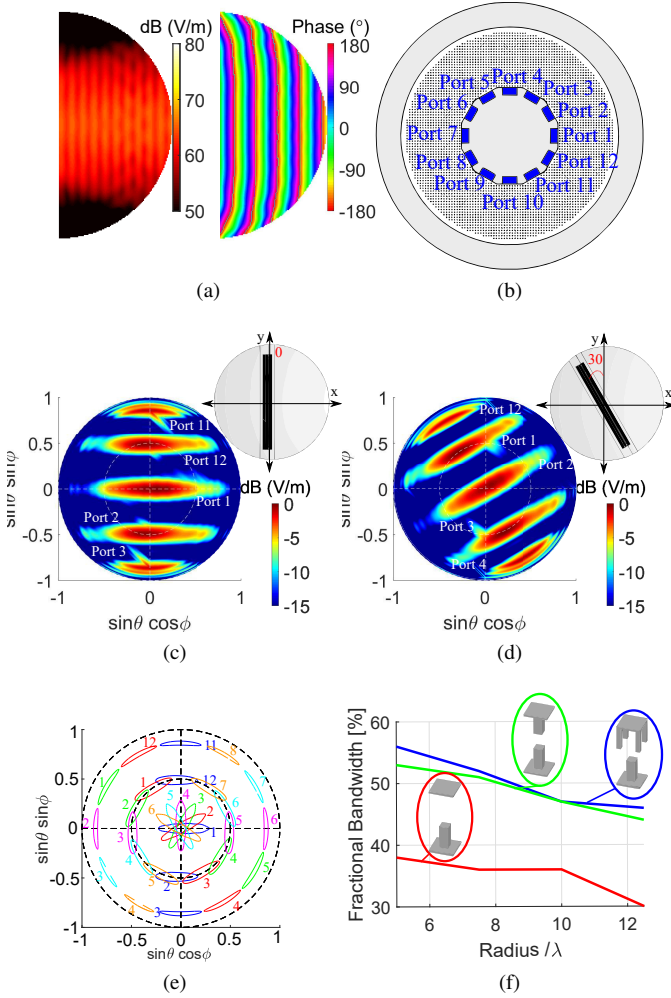


Fig. 3. (a) Magnitude (left) and phase (right) distribution of the vertical component of the electric field (E_z) in logarithmic scale for the top PPW (right) at $f_0 = 31$ GHz when port 1 is excited. (b) Port configuration and numbering in the bottom PPW. Simulated directivity contours in the u - v plane for the 5 fan beams generated at $f = 33$ GHz for: (c) a radiating slot rotated by 0° while exciting ports 11, 12, 1, 2 and 3 and (d) rotated by 30° while exciting ports 12, 1, 2, 3 and 4. (e) Simulated -3 dB directivity contours when the slot is rotated an angle of 0° (blue), 30° (red), 60° (green), 90° (magenta), 120° (cyan) and 150° (orange). In each configuration, a total of 5 beams are generated by the excitation of the corresponding feeds. (f) Fractional BW (for a directivity drop smaller than -3 dB and $SLL \leq -15$ dB) versus the lens' radius for the RLL implemented: with the conventional unit cell (—), with mirror symmetry (—) and with glide symmetry (—).

The operational BW of the lens is defined as the frequency band where the directivity is at most 3 dB lower than the peak value and the SLLs are smaller than or equal to -15 dB. The designed lens respects these requirements from 24 GHz to 43 GHz, yielding a fractional BW of $\approx 56\%$. The same structure implemented with the more conventional bed of nails provides a fractional BW $\approx 36\%$ from 25 GHz to 36 GHz.

The effect of the glide symmetric unit-cell on the RLL implementation is especially apparent in the upper end of the operation band, as we could expect from the profile dispersion of the conventional unit-cell in Fig. 2(b). This results in a slight upscale of the central frequency of operation of the lens from 31 GHz to 33 GHz, which will be taken into account for the following design. In addition, the peak directivity of the lens is slightly increased (from 19.9 dBi to 20.6 dBi)

TABLE I
FEEDING STRUCTURE DIMENSIONS

Variable	l_1	l_2	l_3	l_4	a
Value [mm]	3.6	3.356	2.8	2	7.112
Variable	h_1	h_2	h_3	b	-
Value [mm]	1	0.9	1.93	3.556	-

when using glide symmetries. Further simulations of the RLL were completed for increasing lens radii from $5\lambda_0$ to $12.5\lambda_0$. Fig. 3(f) represents the fractional BW (for a directivity drop smaller than -3 dB and $SLL \leq -15$ dB) as a function of the lens' radius. The blue and green lines stand for the RLLs implemented by the glide symmetry and mirror symmetry unit-cell respectively, while the red one represents the structures realized by the conventional BoN. One can conclude that this BW improvement is maintained for larger radii. And this despite the fact that the longer ray paths in electrically larger lenses introduce larger phase errors as one moves away from the design frequency. Indeed, the use of higher symmetries enables a $\approx 45\%$ BW for a $12.5\lambda_0$ radius.

V. EXPERIMENTAL RESULTS

To validate the previous results, a simplified structure has been realized; it consists of a half-lens with the source placed at the inner focal region. At Ka-band, one could use either metal additive manufacturing [19] or CNC milling [26] to fabricate the metal-only MTS lens. CNC milling of an aluminum block ($\sigma = 3.8 \times 10^7$ S/m) has been selected to benefit from a better surface finish. Fig. 4(a) shows the exploded view of the structure at hand. The radius of the lens, the PPW height and the dimensions of the corner reflector are maintained as $R = 50$ mm, $d = 3.5$ mm and $d_h = 2.5$ mm. The structure radiates through a slot of length $L = 105$ mm and width $W = 10.21$ mm, as in Section IV. The total structure, which includes the stepped waveguide feeder, the top PPW and the radiating slot, has a thickness of 23.7 mm. The thickness $t = 3$ mm of the middle metal plate is crucial to obtain a structure that is stiff enough to enable the milling of the top pillars. The GRIN medium corresponds to the higher symmetric BoN in the bottom PPW. The dimensions of the unit-cell are the same as in Section II. Finally, Fig. 4(b) shows the feeding structure, which includes an E-plane bend and two matching sections. The dimensions of these sections have been optimized (see Table I) to match the input WR-28 waveguide to the open-ended waveguide acting as primary feed.

The final structure comprises the four blocks shown in Fig. 4, which guarantee an easy assembly and alignment. Parts #1 and #2 are used to implement the bottom PPW and the RLL GRIN medium, whereas parts #3 and #4 constitute the top PPW and the radiating long slot. The bottom-left region of Fig. 4(a) shows the CAD model, while the insets display pictures of each part. The dowel pins, marked in Fig. 4(a), ensure the alignment between the 4 blocks, while screws are used to hold together the parts. The feeding waveguide along with the matching sections were carved into block #1 via electrical discharge machining (EDM) using two graphite electrodes: one for the horizontal section with length l_1 and the other one (shown in the bottom-right inset in Fig. 4(a)) for the vertical stepped section in Fig. 4(b). EDM constitutes a

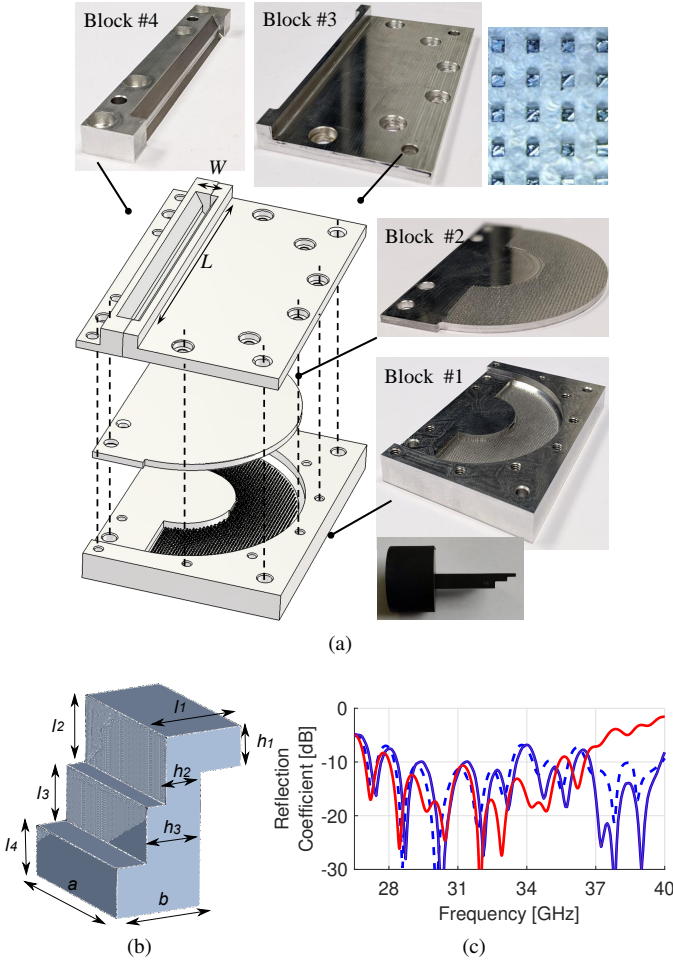


Fig. 4. (a) Fabricated antenna consisting of 4 structural blocks. The top right inset shows the metallic pins, while the bottom right inset shows the electrode used for the EDM process of the feeder. (b) Feeding structure of the antenna. (c) Reflection coefficient comparison between the simulation of the original design (—), the simulation of the realized structure (—) and the measurements (---) at Ka-band.

simple way of machining the l_1 section and allows one to deal accurately with the large aspect ratio $(l_2 + l_3 + l_4)/h_2 = 9.1$ in the stepped waveguide section, which cannot be handled by standard milling drills with diameter h_2 . Moreover, this strategy eliminates the need of additional parts for the feeder.

The red line in Fig. 4(c) represents the simulated input reflection coefficient, optimized to be below -10 dB between 27 GHz and 36 GHz. However, during the EDM fabrication process, the values for the dimensions l_2 and l_4 were swapped by mistake in the final vertical electrode. The continuous and dashed blue lines in Fig. 4(c) depict the simulated and measured input reflection coefficient for the fabricated structure, respectively. Simulations and measurements display a good agreement, there is just a slight frequency shift between curves below 37 GHz. Beyond that frequency, the different levels are attributed to fabrication errors.

The far-field patterns of the prototyped antenna are presented in Fig. 5. Figs. 5(a), (b) and (c) show the simulated and measured normalized directivity patterns in the H-plane at 27 GHz, 33 GHz and 39 GHz, respectively. A good agreement is noticed between the simulated (solid blue line) and measured (dashed blue line) results, with slight mismatches

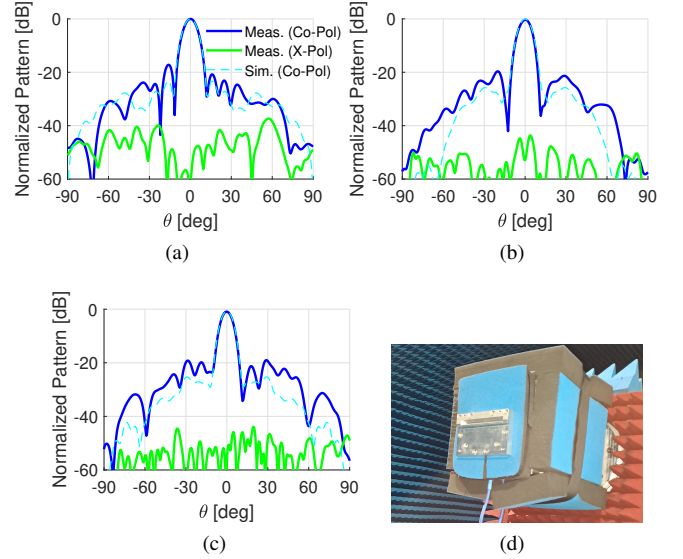


Fig. 5. Comparison between the simulated (---) and measured (—) normalized H-plane directivity patterns at (a) 27 GHz, (b) 33 GHz and (c) 39 GHz for the lens in Fig. 4. The measured cross-polarized pattern (—) is also shown in each sub-figure. (d) Radiation pattern measurement set-up.

regarding the side lobe levels and their symmetry. In turn, the measured cross-polarized component of the directivity (dashed green line) remains well below -40 dB for all frequencies.

The directivity and SLL versus frequency are depicted in Fig. 6(a) and Fig. 6(b), respectively. The blue curves present the simulated performance of the final design, while the red lines stand for its conventional counterpart. A stable operation of the designed lens is observed throughout the entire Ka-band, with an average simulated directivity of 19.86 dBi and peak directivity 21.4 dBi. The simulated SLLs remain below -18.2 dBi for all the frequencies, while the fractional BW of the antenna (abiding to a directivity drop no larger than 3 dB and $SLL \leq -15$ dB) is $\approx 56\%$ extending wider than the Ka-band. These results are also validated by the data from the measured far-field patterns, which are depicted with a black dotted line and show an excellent agreement up to 40 GHz. The same structure designed with the conventional BoN operates only between 26 GHz and 36 GHz with average and peak directivity values of 19.01 dBi and 20.2 dBi, respectively, and a BW of $\approx 36\%$. Fig. 6(c) shows the gain and directivity as a function of frequency, simulated and measured results are in good agreement. The simulated average radiation efficiency is 92.4%, whereas the measurements yield a slightly lower 87.35% average efficiency. These results substantiate the analysis in Section IV, showing a BW increase and, notably, a more stable performance for the higher symmetric BoN. This improvement comes at the expense of an increased fabrication complexity, which could be mitigated by resorting to metal additive manufacturing. Finally, taking into account the measured input reflection coefficient, gives an overall BW of $\approx 39\%$ with amendment for small sub-bands where the matching is slightly above -10 dB.

VI. CONCLUSION

The realization of metal-only reflecting Luneburg lenses (RLLs) by bed of nails (BoN) metasurface has been discussed.

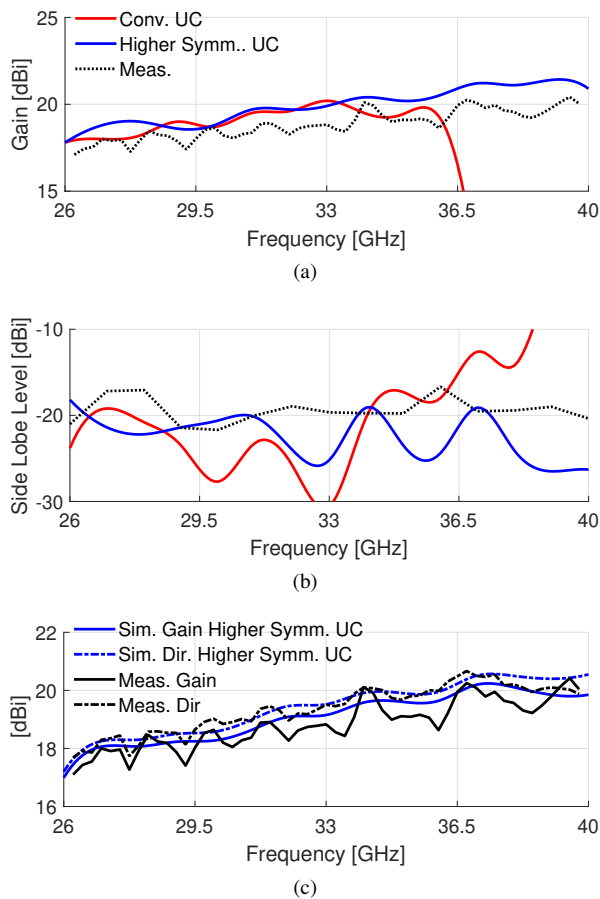


Fig. 6. (a) Gain and (b) SLL versus frequency for the RLL simulated with (—) and without (—) higher symmetries and measured values for the higher symmetry case (·····). (c) Measured (black) and simulated (blue) gain and directivity versus frequency curves.

We have shown that the relatively high equivalent refractive indexes in RLLs can be easily obtained by introducing higher symmetries in the BoN structure. This approach comes with the additional benefit of significantly increasing the operational bandwidth (BW). A lens has been fabricated and measured providing good agreement with simulations. The operational BW of the lens allows one to cover practically the whole Ka-band, and the measured fractional BW of $\approx 39\%$ is wider than that predicted for the conventional BoN counterpart while also providing a more stable performance.

ACKNOWLEDGMENT

The authors are grateful to Dr. L. Le Coq (M2ARS, IETR) for the radiation pattern measurements and Dr. J. Ruiz García (University of Michigan, Ann Arbor) for useful discussions.

REFERENCES

- [1] H. Tataria, M. Shafi, A. F. Molisch, M. Dohler, H. Sjöland, and F. Tufvesson, "6G wireless systems: Vision, requirements, challenges, insights, and opportunities," *Proc. IEEE*, vol. 109, no. 7, pp. 1166–1199, 2021.
- [2] T. Chaloun, L. Boccia, E. Amieri, M. Fischer, V. Valenta, N. J. G. Fonseca, and C. Waldschmidt, "Electronically steerable antennas for future heterogeneous communication networks: Review and perspectives," *IEEE J. Microw.*, vol. 2, no. 4, pp. 545–581, 2022.
- [3] M. Ettore, R. Sauleau, and L. Le Coq, "Multi-beam multi-layer leaky-wave SIW pillbox antenna for millimeter-wave applications," *IEEE Trans. Antennas Propag.*, vol. 59, no. 4, pp. 1093–1100, Apr. 2011.

- [4] R. K. Luneburg, *Mathematical Theory of Optics*. Berkeley, CA, USA: Univ. California Press, Dec. 1964.
- [5] Y. J. Park, A. Herschlein, and W. Wiesbeck, "A photonic bandgap (PBG) structure for guiding and suppressing surface waves in millimeter-wave antennas," *IEEE Trans. Microw. Theory Tech.*, vol. 49, no. 10, pp. 1854–1859, Oct. 2001.
- [6] X. Wu and J.-J. Laurin, "Fan-beam millimeter-wave antenna design based on the cylindrical Luneberg lens," *IEEE Trans. Antennas Propag.*, vol. 55, no. 8, pp. 2147–2156, 2007.
- [7] P. Bantavis, C. Garcia-Gonzalez, R. Sauleau, G. Goussetis, S. Tubau, and H. Legay, "Broadband graded index Gutman lens with a wide field of view utilizing artificial dielectrics: A design methodology," *Opt. Express*, vol. 28, no. 10, pp. 14 648–14 661, 2020.
- [8] F. Doucet, N. J. Fonseca, E. Girard, X. Morvan, L. Le Coq, H. Legay, and R. Sauleau, "Shaped continuous parallel plate delay lens with enhanced scanning performance," *IEEE Trans. Antennas Propag.*, vol. 67, no. 11, pp. 6695–6704, Nov. 2019.
- [9] T. Ströber, S. Tubau, E. Girard, H. Legay, G. Goussetis, and M. Ettore, "Shaped parallel-plate lens for mechanical wide-angle beam steering," *IEEE Trans. Antennas Propag.*, vol. 69, no. 12, pp. 8158–8169, 2021.
- [10] Y. B. Li, R. Y. Wu, W. Wu, C. B. Shi, Q. Cheng, and T. J. Cui, "Dual-physics manipulation of electromagnetic waves by system-level design of metasurfaces to reach extreme control of radiation beams," *Adv. Mater. Technol.*, vol. 2, no. 1, p. 1600196, 2017.
- [11] J. Ruiz-García, E. Martini, C. D. Giovampaola, D. González-Ovejero, and S. Maci, "Reflecting Luneburg lenses," *IEEE Trans. Antennas Propag.*, vol. 69, no. 7, pp. 3924–3935, Jul. 2021.
- [12] Q. Chen, S. A. R. Horsley, N. J. G. Fonseca, T. Tyc, and O. Quevedo-Teruel, "Double-layer geodesic and gradient-index lenses," *Nat Commun*, vol. 13, no. 1, p. 2354, Dec. 2022.
- [13] C. Bilitos, J. Ruiz-García, R. Sauleau, E. Martini, S. Maci, and D. González-Ovejero, "Higher-symmetries for broadband reflecting luneburg lenses at ka-band," in *16th Eur. Conf. on Antennas Propag. (EuCAP)*, 2022, pp. 1–3.
- [14] C. Bilitos, X. Morvan, E. Martini, R. Sauleau, S. Maci, and D. González-Ovejero, "Broadband reflecting luneburg lens beam-former at ka-band," in *Int. Conf. Numer. Electromagn. Multiphys. Model. Optimization (NEMO)*, 2022, pp. 1–4.
- [15] P. Crepeau and P. McIsaac, "Consequences of symmetry in periodic structures," *Proc. IEEE*, vol. 52, no. 1, pp. 33–43, 1964.
- [16] A. Hessel, Ming Hui Chen, R. Li, and A. Oliner, "Propagation in periodically loaded waveguides with higher symmetries," *Proc. IEEE*, vol. 61, no. 2, pp. 183–195, 1973.
- [17] O. Quevedo-Teruel, M. Ebrahimpouri, and M. N. M. Kehn, "Ultrawideband metasurface lenses based on off-shifted opposite layers," *IEEE Antennas Wireless Propag. Lett.*, vol. 15, pp. 484–487, Dec. 2016.
- [18] O. Quevedo-Teruel, J. Miao, M. Mattsson, A. Algaba-Brazalez, M. Johansson, and L. Manholm, "Glide-symmetric fully metallic Luneburg lens for 5G communications at Ka-band," *IEEE Antennas Wireless Propag. Lett.*, vol. 17, no. 9, pp. 1588–1592, Sep. 2018.
- [19] D. González-Ovejero, N. Chahat, R. Sauleau, G. Chattopadhyay, S. Maci, and M. Ettore, "Additive manufactured metal-only modulated metasurface antennas," *IEEE Trans. Antennas Propag.*, vol. 66, no. 11, pp. 6106–6114, Nov. 2018.
- [20] O. Quevedo-Teruel, Q. Chen, F. Mesa, N. J. G. Fonseca, and G. Valerio, "On the benefits of glide symmetries for microwave devices," *IEEE J. Microw.*, vol. 1, no. 1, pp. 457–469, Jan. 2021.
- [21] G. Valerio, F. Ghasemifard, Z. Sipus, and O. Quevedo-Teruel, "Glide-symmetric all-metal holey metasurfaces for low-dispersive artificial materials: Modeling and properties," *IEEE Trans. Microw. Theory Tech.*, vol. 66, no. 7, pp. 3210–3223, Jul. 2018.
- [22] A. A. Brazález, L. Manholm, M. Johansson, O. Quevedo-Teruel, and J. Miao, "Investigation of a ka-band luneburg lens made of a glide-symmetric holey structure," in *Int. Symp. Antennas Propag. (ISAP)*, 2017, pp. 1–2.
- [23] D. González-Ovejero, X. Morvan, L. L. Coq, and O. de Sagazan, "Millimeter-wave and sub-thz modulated metasurface antennas," in *Int. Congr. Artif. Mater. Novel Wave Phenomena*, 2020, pp. 281–283.
- [24] CST of America, "CST Microwave Studio," Anaheim, CA, 2020.
- [25] T. Potelon, M. Ettore, T. Bateman, J. Francey, and R. Sauleau, "Broadband passive two-feed-per-beam pillbox architecture for high beam crossover level," *IEEE Trans. Antennas Propag.*, vol. 68, no. 1, pp. 575–580, 2020.
- [26] C. D. Diallo, E. Girard, H. Legay, and R. Sauleau, "All-metal Ku-band Luneburg lens antenna based on variable parallel plate spacing Fakir bed of nails," in *11th Eur. Conf. Antennas Propag.*, Mar. 2017, pp. 1401–1404.